Research Article Vol. 30, No. 14 / 4 Jul 2022 / Optics Express 24655
Optics EXPRESS

Compact and broadband silicon mode-order converter using bricked subwavelength gratings

MENGJIA LU, CHUNYU DENG, YU SUN, DONGYU WANG, LEI HUANG, PENGCHENG LIU, DONGDONG LIN, WEI CHENG, GUOHUA HU, TONG LIN, BINFENG YUN,* AND YIPING CUI

Advanced Photonics Center, Southeast University, Nanjing 210096, China
*ybf@seu.edu.cn

Abstract: A compact and broadband silicon mode-order converter (MOC) scheme by employing reciprocal mode evolution between asymmetric input/output taper and bricked subwavelength gratings (BSWG) is proposed. In the proposed MOC, a quasi-TE_0 mode is generated in the BSWG region, which can be regarded as an effective bridge between the two TE modes to be converted. Flexible mode conversion can be realized by only choosing appropriate structure parameters for specific mode transitions between input/output modes and the quasi-TE_0 mode. By combing 3D finite difference time domain (FDTD) and particle swarm optimization (PSO) method, TE_0-TE_1 and TE_0-TE_2 MOCs are optimal designed, which can efficiently convert TE_0 mode to TE_1 and TE_2 modes with lengths of 9.39 μm and 11.27 μm, respectively. Results show that the insertion losses of <1 dB and crosstalk of <-15 dB are achieved for both TE_0-TE_1 and TE_0-TE_2 MOCs, the corresponding working bandwidth are 128 nm (1511~1639 nm) and 126 nm (1527~1653 nm), respectively. Additionally, the MOCs can be fabricated with only single etch step with minimum feature size of 145 nm.

1. Introduction

Photonic integrated circuit (PIC) is an enabling technology for high-density and cost-effective optical interconnect [1]. Facing with the increasing capacity requirements of on-chip optical interconnects, mode division multiplexing technology, which leverages the different spatial eigenmodes at the same wavelength as independent channels to transmit optical signals, has attracted tremendous interest [2]. Over past years, various mode-division multiplexing (MDM) devices have been demonstrated on the silicon-on-insulator (SOI) platform, such as mode (de) multiplexers [3,4], mode-order converters [5,6], multimode waveguide bends [7,8] and multimode waveguide crossings [9]. Among them, mode-order converters (MOCs) that can convert the fundamental mode to high-order modes are key components in MDM systems.

More recently, a variety of schemes for MOCs have been proposed, including asymmetric direction couplers (ADC) [10], Y-branch [11], Mach-Zehnder interferometer (MZI) [12], waveguide Bragg grating [13], refractive index perturbation structures [14,15], and subwavelength structure [16]. ADC can realize phase matching between the input fundamental mode and output high-order mode, but such device is limited by the relative narrow bandwidth and fabrication tolerances owing to the strict phase matching condition [10]. MZI is commonly used to realize the desired mode conversion by introducing an extra phase shift component between two arms of the MZI structure [12]. Waveguide Bragg grating, a normally employed component in the field of optical sensing system, introducing specified phase shift to achieve the efficient mode conversion [13]. However, all of them suffer from relatively large device lengths (>50 μm), which limits their high-density integration. In order to efficiently shrink the device size, polygonal etching slots and tilted slots are proposed to generate the required refractive index distributions with the conversion lengths of 24 μm [14] and 5.47 μm [15], respectively. In addition, periodic tilted

#462554 https://doi.org/10.1364/OE.462554
Journal © 2022 Received 27 Apr 2022; revised 7 Jun 2022; accepted 13 Jun 2022; published 23 Jun 2022

Optics EXPRESS

subwavelength slots are introduced to realize the conversion between TE_0 and TE_1 modes with the device length of 5.75 μm [16]. However, two-step lithography and high-precision shallow etching processes are required. Besides, prevailing topology optimization [17], inverse design [18], and deep learning [19] methods can also be exploited to achieve the optimal refractive index distributions for mode conversion, while the formed irregular refractive index patterns are not easy for fabrication and the optimization processes are usually time-consuming.

Subwavelength gratings (SWGs), which can tailor the dispersion properties and refractive indices of photonic devices are widely used to achieve broadband operation and reduce device footprints [20–22]. For example, a high-order mode (de) multiplexer was proposed using SWG-based directional couplers, whose insertion loss lower than 5.2 dB in 1520 nm~1570 nm and device footprint is less than 507×5.29 μm^2 [23]. In Ref. [24], an ultra-broadband mode (de)multiplexer composed of three-waveguide coupler based on SWG has been demonstrated with working bandwidth exceeding 300 nm when the mode crosstalk <-15 dB, whose length is about 36.5 μm. In Ref. [25], Sun et al. have reported an ultra-broadband power coupling and mode-order conversion based on trapezoidal SWGs, whose conversion loss and crosstalk are below 1 dB and -12.5 dB, respectively. However, relative long length of 62.5 μm is required due to the adiabatic coupling between waveguides. Generally, it is imperative and challenging to realize mode conversion with a small footprint, low loss, low crosstalk, as well as broad working bandwidth. In addition, employing the full potential of SWGs is also challenging with current wafer-scale fabrication technologies. Recently, a bricked subwavelength grating (BSWG) which can synthesize a tailorable biaxial crystal with control over its anisotropy and dispersion has been proposed to alleviate the strict fabrication requirements of the conventional SWG structures [26].

In this work, we propose a compact silicon-based MOC scheme by employing BSWG connected with asymmetric input/output waveguide tapers that can convert the fundamental TE mode to high order TE modes. In the proposed MOC, a quasi-TE_0 mode is generated in the BSWG region, which can be regarded as an effective bridge between the two TE modes to be converted. In addition, benefiting from the lower dispersion of BSWG compared with traditional SWG, broad working bandwidth is achieved. As a proof of concept, two MOCs that can convert TE_0 mode to TE_1 (TE_2) mode are optimal designed by using the particle swarm optimization (PSO) method. For the TE_0-TE_1 MOC, the device length is 9.39 μm, the working bandwidth is 128 nm (1511~1639 nm) when the insertion loss is lower than 1 dB and the crosstalk is below -15 dB. For the TE_0-TE_2 MOC, the device length is 11.27 μm, whose working bandwidth is 126 nm (1527~1653 nm) when the insertion loss is lower than 1 dB and the crosstalk is below -15 dB.

2. Structure and principle

Figure 1 depicts the three-dimensional (3D) and 2D schematic of the proposed MOC, as well as part enlarged view of the BSWG. Here, the device involves three parts, including the Taper1, Taper2 and the BSWG. The input waveguide Taper1 is tapered from $w_1 = 500$ nm to $w_s = 145$ nm in a length of L_{tp1} and the output waveguide Taper2 is tapered from w_4 to w_3 in a length of L_{tp2}. The position of Taper2 is denoted by the length of w_p as shown in Fig. 1(b). The BSWG is composed of alternating strips of the Si and SiO_2 arrayed with a subwavelength period $\Lambda_z = 290$ nm along the propagation direction (z-axis), the Si strips are periodically partitioned along the x-axis with a period $\Lambda_x = 290$ nm, and the resulting Si blocks are then alternately shifted by a distance Δz in the z-direction. The duty cycles in the x and z directions are defined as $f_x = a_x/\Lambda_x = 0.5$ and $f_z = a_z/\Lambda_z = 0.5$, respectively, as it can produce the largest pixel dimensions (145×145 nm^2). The silicon wire width a in the BSWG is equal to a_x and a_z, represented by $a = a_x = a_z$. The thickness of silicon is 220 nm and the refractive indices of Si and SiO_2 at λ=1550 nm are taken as 3.476 and 1.444, respectively. The whole device is covered by SiO_2 claddings.

The proposed device operates in the deep subwavelength regime, that is to say $\Lambda << \lambda$. According to the Rytov formulas, the equivalent refractive indices of the conventional SWG can

Optics EXPRESS

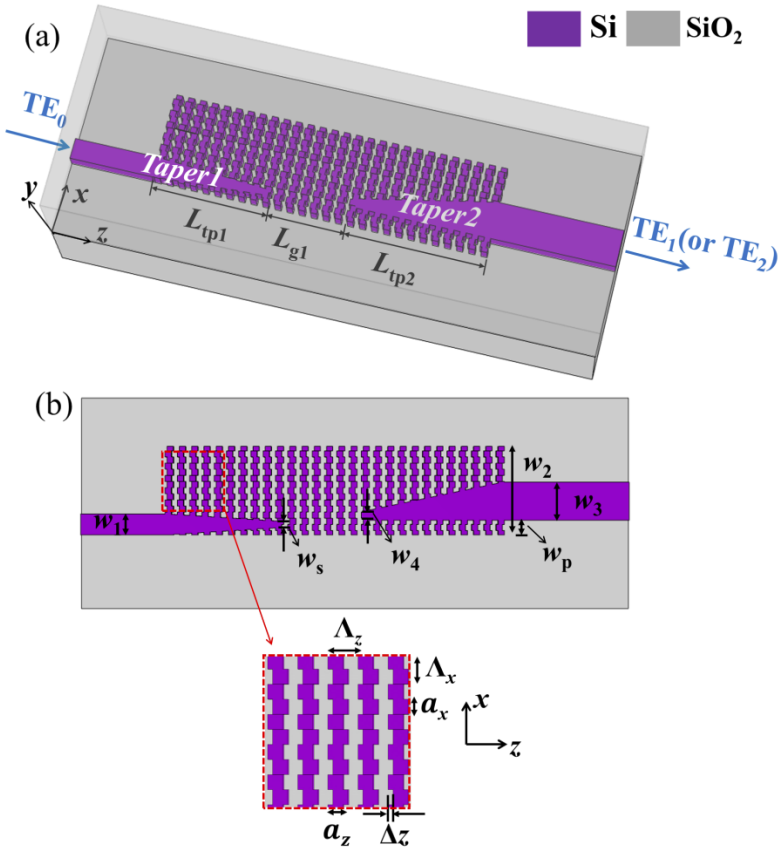

Fig. 1. (a) 3D view of the proposed MOC; (b) 2D view of the proposed MOC and part enlarged view of the BSWG.

be calculated by [27]:

$$n_{//} = [f_x n_{Si}^2 + (1 - f_x) n_{SiO2}^2]^{1/2} = 2.66 \tag{1}$$

$$n_{\perp} = [f_x n_{Si}^{-2} + (1 - f_x) n_{SiO2}^{-2}]^{-1/2} = 1.89 \tag{2}$$

where $n_{||}$ and $n_{\perp}$ represent polarization parallel/perpendicular to z-direction, respectively. Here, a full-vectorial mode solver based on finite-difference frequency-domain (FDFD) method is employed to investigate the characteristics of the waveguide taper embedded in the BSWG, in which the BSWG is treated as a homogenous anisotropic medium, thus the equivalent refractive index of the BSWG n_{BSWG} can be represented by its diagonal refractive index tensor ($\overline{\Delta z}$) [26]:

$$n_{\mathrm{BSWG}} = \mathrm{diag}[n_{xx}(\overline{\Delta z}), n_{//}, n_{zz}(\overline{\Delta z})] \tag{3}$$

where $\overline{\Delta z}$=$\Delta z/\Lambda_z$. The equivalent refractive index $n_{xx}(\overline{\Delta z})$ and $n_{zz}(\overline{\Delta z})$ can be expressed as [26]:

$$n_{xx}(\overline{\Delta z}) = A + B\cos(2\pi\overline{\Delta z}) \tag{4}$$

$$n_{zz}(\overline{\Delta z}) = n_{\perp} n_{\parallel} [A + B\cos(2\pi\overline{\Delta z})]^{-1} \tag{5}$$

where $A = 0.5\left(n_{\parallel} + \sqrt{n_{\parallel} n_{\perp}}\right)$, $B = 0.5\left(n_{\parallel} - \sqrt{n_{\parallel} n_{\perp}}\right)$. For the case when $\overline{\Delta z} = 0$, it represents a conventional SWG structure, whose refractive index tensor is given by: $n_{xx}(0)$=$n_{//}$ and $n_{zz}(0)$= $n_{\perp}$.

Optics EXPRESS

Figure 2 depicts the working principle of the proposed device. Figure 2(a) shows the top view of theTaper2 and BSWG region and Fig. 2(b) shows cross-section view of the Taper2 embedded in the BSWG, which can be regarded as a silicon waveguide inserted between two BSWG regions. Figure 2(c) and Fig. 2(d) show the effective indices and the corresponding field profiles (E_x) vary as the Taper2's width w_{tp} for the TE_1-to-TE_0 MOC and the TE_2-to-TE_0 MOC under the condition of $\overline{\Delta z}$= 0.16, respectively. As shown in Fig. 2(c) and (d), the modal field of TE_1 (TE_2) closed to the tapering boundary is gradually squeezed out and enhanced at the interface between the Taper2 and the BSWG when w_{tp} decreases. Then the extruded modal field is separated from the Taper2 and guided as a quasi-TE_0 mode in the BSWG region. Moreover, explanations of such a mode evolution process from a single-mode like component into higher-order modes can be found in Ref. [28]. To demonstrate the mode evolution process for TE_1 (TE_2) mode to quasi-TE_0 mode, three-dimensional finite difference time domain (3D FDTD) simulations are performed and the results are shown in Fig. 2(e) and Fig. 2(f). It can be seen that the injected TE_1 (TE_2) mode is gradually transferred to the quasi-TE_0 mode from the Taper2 into the BSWG region when the Taper2 is narrowed from 0.9 μm to 0.2 μm (1.4 μm to 0.2 μm), which is consistent with mode analysis shown in Fig. 2(c) and Fig. 2(d). And the transition lengths for TE_1 (TE_2)

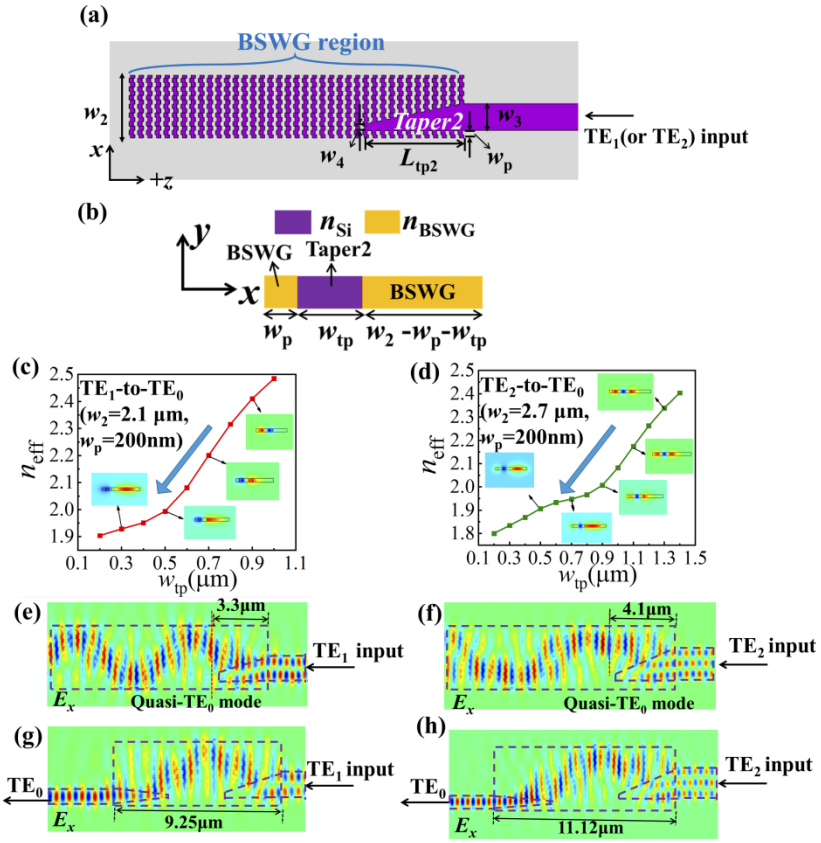

Fig. 2. Working principle for the proposed device (a) Top view and geometrical parameters of the Taper2 and BSWG region; (b) Cross-section view of the Taper2 embedded in the BSWG; Effective indices and corresponding field profiles (E_x) vary as the Taper2's width w_{tp} for (c) TE_1-to-TE_0 MOC and (d) TE_2-to-TE_0 MOC; Simulated major component (E_x) of TE mode field evolutions when input (e) TE_1 mode and (f) TE_2 mode; Mode field evolutions of (g) TE_1-to-TE_0 and (h) TE_2-to-TE_0 mode-order conversions.

Optics EXPRESS

mode to quasi-TE_0 mode are about 3.3 μm and 4.1 μm, respectively. Based on the same mode evolution processes, the TE_1-to-TE_0 and TE_2-to-TE_0 mode-order conversion can be obtained by introducing another Taper1 in the other side of the BSWG region to collect the quasi-TE_0 mode in the BSWG and then convert it to the TE_0 mode of the Taper1, as shown in Fig. 2(g) and Fig. 2(h).

Here, to illustrate the advantages of BSWG comparing with traditional SWG, we take the TE_0-TE_1 MOC as an example. The optimized width of BSWG w_2= 2.1 μm. Figure 3 shows the mode effective indices of the TE_0 Floquet-Bloch modes propagating along the z-axis when $\overline{\Delta z} = 0$ and $\overline{\Delta z} \neq 0$, calculated by 3D FDTD method for photonic structures [29]. It should be noted that TE_0 Floquet-Bloch mode here is different from the quasi-TE_0 mode in Fig. 2. TE_0 Floquet-Bloch mode is the eigenmode in the BSWG while the quasi-TE_0 mode is a TE_0-like mode, which is similar with the TE_0 Floquet-Bloch mode generated in the mode evolution process. The optimized shifting value $\overline{\Delta z}$= 0.16 for the TE_0-TE_1 MOC is obtained by using the particle swarm optimization method and the details are discussed in the following part. As shown in Fig. 3, it is obviously that the mode effective index and the dispersion of the TE_0 Floquet-Bloch mode are reduced when $\overline{\Delta z} \neq 0$ is introduced. Compared with conventional SWG (minimum feature size of ~100 nm), the BSWG also has a uniform grid and pixel dimensions as large as 145×145 nm^2 in the near-infrared band. Generally, the introduction of the BSWG decreases the wavelength dependence of the mode effective index, which is benefit to broadband working and can alleviate the fabrication difficulty.

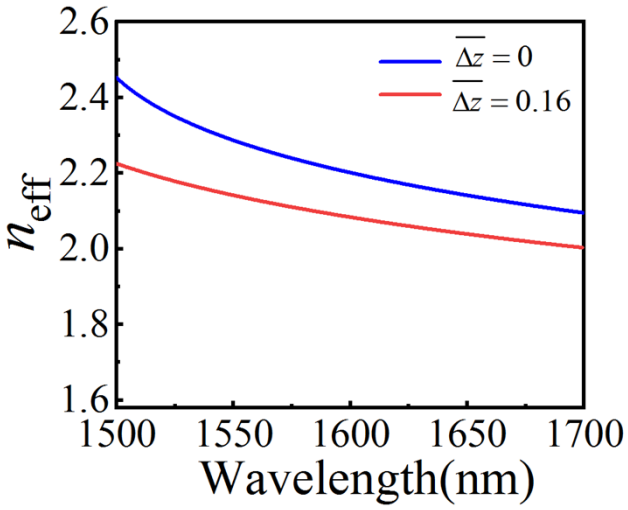

Fig. 3. Calculated mode effective indices of the TE_0 mode as $\overline{\Delta z}$ varies for the TE_0-TE_1 MOC.

3. Results and discussion

In order to optimize the proposed MOC with BSWG based on mode evolution and conversion, the structure parameters (w_2, w_3, w_4, w_p, L_{tp1}, L_{tp2}, L_{g1}, $\overline{\Delta z}$) shown in Fig. 1 has been optimized at the wavelength of 1.55 μm by combing 3D FDTD and PSO methods. The figure of merit (FOM) is defined as:

$$\text{FOM} = -10\log\left(\frac{P_{TE_i}}{P_{in}}\right) \tag{6}$$

where i = 1 or 2, P_{TEi} represents the optical power of TE mode obtained at the output waveguide.

Optics EXPRESS

To simply illustrate the optimization process, we take TE_0-TE_1 MOC as an example. A TE_0-TE_1 MOC with a specific combination of parameters is represented as a "particle". The particle's position and velocity can be updated by utilizing the equations given below [30]:

$$ve_{j+1} = \omega \times ve_j + r_1 \times rand() \times (bp_j - ps_j) + r_2 \times rand() \times (gp_j - ps_j) \tag{7}$$

$$ps_{j+1} = ps_j + ve_j \tag{8}$$

where ve_j (j = 1, 2,. . .) and ps_j represent the particle's velocity and position, g_{pj} and b_{pj} stand for the global best position and the individual best position, rand() is a random number uniformly distributed between 0 and 1, r_1 and r_2 are cognitive rate and social rate, the inertial weight is denoted by ω. To start optimizing, we initialize particle's *ps* and vectors *ve*, where *ps* correspond to [w_2, w_3, w_4, w_p, L_{tp1}, L_{tp2}, L_{g1}, $\overline{\Delta z}$] and *ve* represents the variation of *ps* after one iteration. First, the particles in the swarm are selected as random values for 1.8 μm ≤ w_2≤2.5 μm, 0.8 μm ≤ w_3≤1.2 μm, 0.15 μm ≤ w_4≤0.35 μm, 0 μm ≤ w_p≤0.8 μm, 1 μm ≤ L_{tp1}≤3 μm, 1 μm ≤ L_{tp2}≤4 μm, 2 μm ≤ L_{g1}≤4 μm and 0≤$\overline{\Delta z}$≤0.5. Regarding the searching range of the structural parameters, the descriptions are as follows: (1) the widths of w_2, w_3 and w_4 should be not too wide or too narrow to obtain the trade-off between the desired TE_1 mode and the undesired TE_2 mode and TE_0 mode. In addition, as shown in Fig. 5, the searching range of w_p should be smaller than w_2-w_3. (2) the lengths of L_{tp1}, L_{g1} and L_{tp2} should be neither too long or too short owing to the trade-off between mode propagation loss and compact device footprint. (3) the maximum value of deviation Δz is the width of silicon wire waveguide a_z, which is half of Λ_z. According to $\overline{\Delta z}$=$\Delta z/\Lambda_z$, the maximum $\overline{\Delta z}$ is 0.5. And the minimum value is 0, corresponding to conventional SWG. Next, the specific optimization steps are illustrated in Fig. 4. In the simulation, ω, r_1 and r_2 were chosen as ω=1, r_1 = 2, and r_2 = 2, respectively. The swarm population is chosen as 20. In the optimization process of TE_0-TE_2 MOC, the only difference is the searching range of the particles, which are 2.5 μm ≤ w_2≤3 μm, 1.3 μm ≤ w_3≤1.6 μm, 0.15 μm ≤ w_4≤0.35 μm, 0 μm ≤ w_p≤0.8 μm, 1 μm ≤ L_{tp1}≤4 μm, 1 μm ≤ L_{tp2}≤4 μm, 2 μm ≤ L_{g1}≤7 μm and 0≤$\overline{\Delta z}$≤0.5. Figure 5 shows the FOMs as a function of the number of iterations in the optimization processes of TE_0-TE_1 and TE_0-TE_2 MOCs. According to Eq. (6), the smaller the FOM obtained, the higher the conversion efficiency can be achieved. As shown, the FOMs for the designed two MOCs drop fast in about 15 iterations and reach the minimum after 20 iterations. Finally, the optimized parameters are listed in Table 1.

Table 1. Optimized design parameters for the proposed MOCs

Mode converter	w_2(μm)	w_3(μm)	w_4(nm)	w_p(nm)	L_{tp1}(μm)	L_{tp2}(μm)	L_{g1}(μm)	$\overline{\Delta z}$
TE_0-TE_1	2.1	0.9	229	0	3	3.2	3.19	0.16
TE_0-TE_2	2.67	1.4	350	373	3.21	4.0	4.06	0.14

The electric field distributions of TE_0-TE_1 and the TE_0-TE_2 MOCs are simulated and shown in Fig. 6. It can be seen from Fig. 6(a) that the incident TE_0 mode can be converted to the TE_1 mode with a conversion length of 9.39 μm. To verify the scalability of our proposed structure, a TE_0-TE_2 MOC is also demonstrated as shown in Fig. 6(b), where the launched TE_0 mode can be converted to TE_2 mode with a conversion length of 11.27 μm.

Figure 7 (a) and (b) show the transmission spectra of the proposed TE_0-TE_1 and TE_0-TE_2 MOCs, in which all the supported eigenmodes are listed. For the TE_0-TE_1 MOC, the TE_0-TE_1 mode conversion loss is lower than 1 dB and the crosstalk is below -15 dB in the wavelength range of 1511 nm~1639 nm, including S, C, L and U band. For the TE_0-TE_2 MOC, the TE_0-TE_2 mode conversion loss is lower than 1 dB and the crosstalk is below -15 dB in the wavelength range of 1527 nm~1653 nm, including S, C, L and U band. Concerning about the transmission responses in Fig. 7, the mode conversion loss drops and the crosstalk increases quickly at the short

Optics EXPRESS

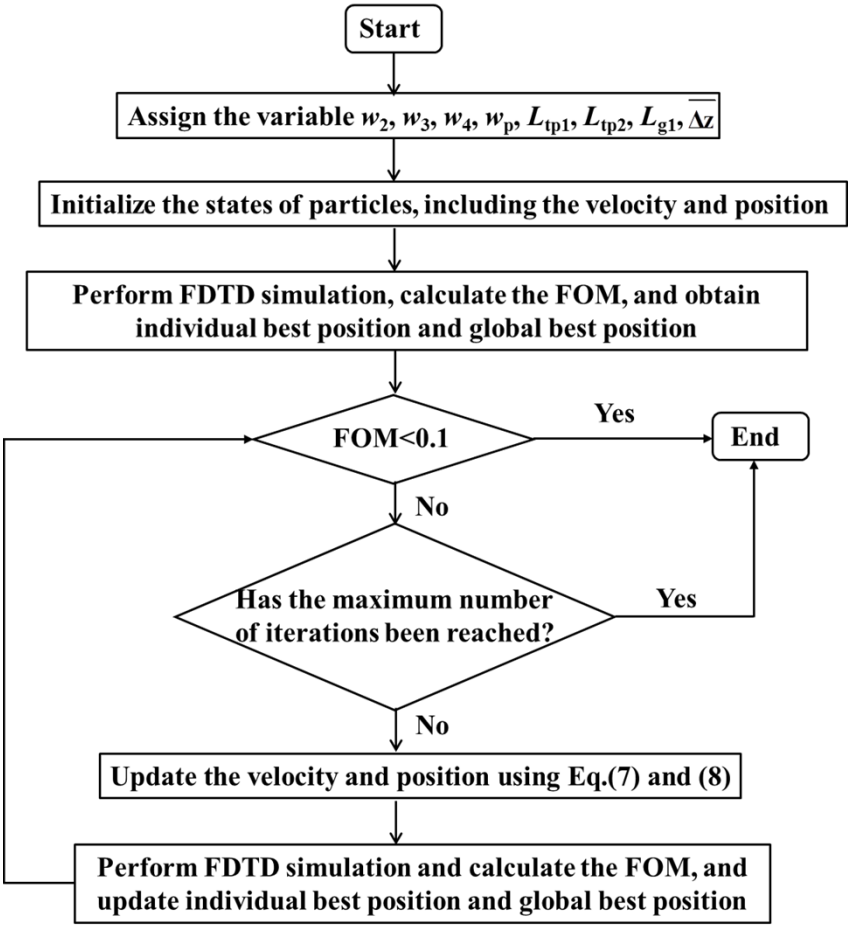

Fig. 4. Flow chart of the optimization process.

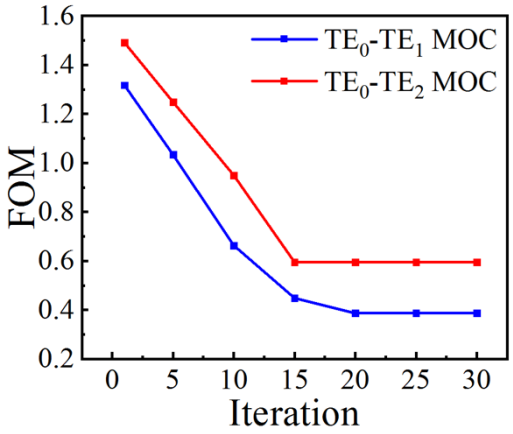

Fig. 5. FOM changing with the number of iterations for the TE_0-TE_1 MOC and the TE_0-TE_2 MOC

Optics EXPRESS

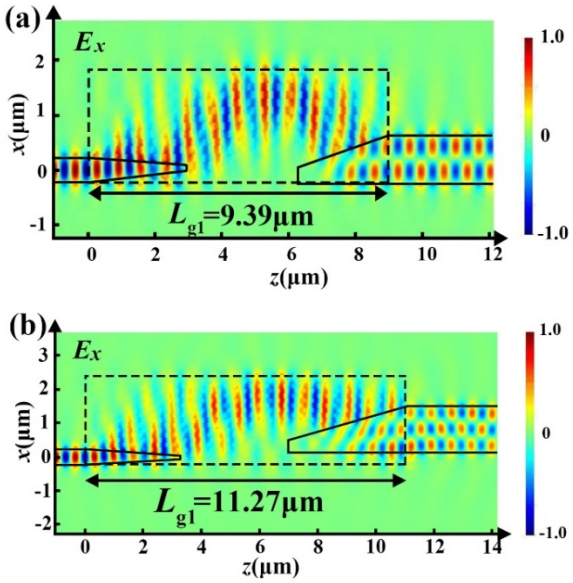

Fig. 6. Electric-field evolution with the simulated E_x distribution for the proposed (a) TE_0-TE_1 MOC and (b) TE_0-TE_2 MOC.

wavelength margin near 1500 nm. These are caused by Bragg reflection since the wavelength is getting close to the Bragg wavelength.

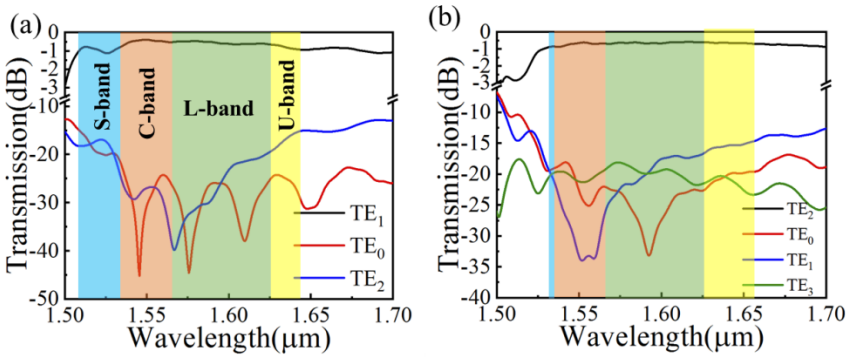

Fig. 7. Simulated transmission spectra of the (a) TE_0-TE_1 MOC and (b) TE_0-TE_2 MOC.

In order to investigate the fabrication tolerances of the proposed MOCs, we have simulated the transmission responses of the proposed device with the deviation of Taper1 tip width Δw_s, Taper2 tip width Δw_4, silicon wire width Δa and shifting δz in the BSWG at λ=1.55 μm as shown in Fig. 8. Specially, the variation of shifting Δz is denoted by δz. For the TE_0-TE_1 MOC, the insertion losses are < 1.5 dB and the crosstalk are <-10 dB within the range of -50 nm $<\Delta w_s<$ 50 nm, -100 nm$<\Delta w_4<$ 100 nm and -14 nm $<\Delta a<$ 10 nm, - 13 nm $<\delta z<$ 11 nm. For the TE_0-TE_2 MOC, in the range of -50 nm $<\Delta w_s<$ 50 nm, -100 nm$<\Delta w_4<$ 100 nm and -8 nm $<\Delta a<$ 10 nm, -14 nm$<\delta z<$ 9 nm the insertion losses are < 2 dB and the crosstalk are <-9 dB. The proposed device allows a relatively large fabrication tolerance and shows good potential for the large-scale fabrication.

Optics EXPRESS

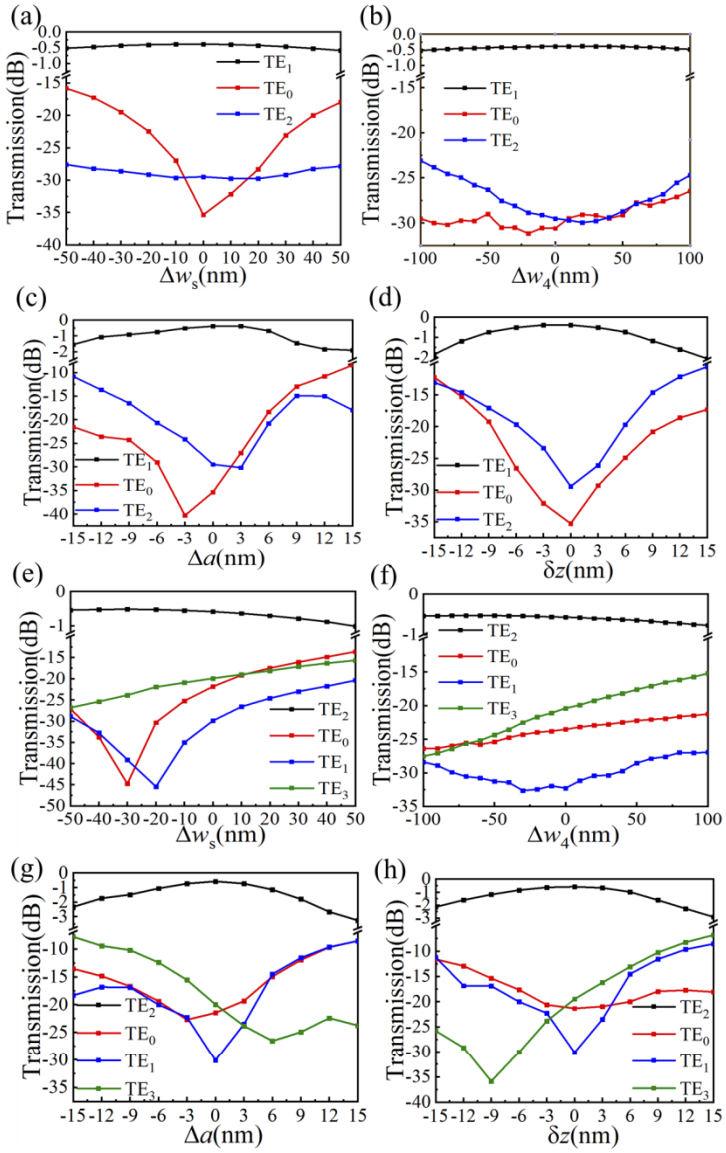

Fig. 8. The transmission spectra by changing the variations of width (Δw_s, Δw_4, Δa, δz) for the proposed (a-d) TE_0-TE_1 MOC and (e-h) TE_0-TE_2 MOC.

Optics EXPRESS

Table 2 compares our proposed structures with several reported MOCs. It shows that our work has greatly broadened the working bandwidth by introducing of the BSWG with low dispersion. Compared with Ref. [28], our device has larger minimum feature size of 145 nm, smaller lowest crosstalk <-20 dB at 1.55 μm as well as broader bandwidth >125 nm, as shown in Fig. 7. Meanwhile, our scheme can flexibly achieve fundamental mode to high-order modes with compact device size, low insertion loss, low crosstalk, as well as broad working bandwidth.

Table 2. Comparison of various MOCs.[a]

Structure	Function	Device length (μm)	CE (%)	CT (dB)	IL (dB)	Bandwidth (nm)	MFS (μm) &N	E/S
MZI [12]	TE_0-TE_1	>50	/	<-24	<1	35(CT<-24dB)	/ &1	E
Bragg grating [13]	TE_0-TE_1	~130	/	<-19	/	9(IL < 3dB)	0.15 &2	E
Ploygonal etching slot [14]	TE_0-TE_1	~24	>97.6	<-20	/	100	0.86 &2	S
	TE_0-TE_2	~8	/	/	/	(CT<-20dB&CE > 97.6%)	&2	
Tilted slot [15]	TE_0-TE_1	5.47	95	<-20	/	/	1	S
	TE_0-TE_2	7.23	83	<-15	/		&2	
Tilted metasurface [16]	TE_0-TE_1	5.75	78	<-12.5	<1	20	0.2	E
	TE_0-TE_2	6.74	70	<-12.8	<1	(IL < 1dB&CT<-10dB)	&2	
SWG [28]	TE_0-TE_1	4.1	>80	<-10	<1	~100	0.1	S
	TE_0-TE_2	5.9				(IL < 1dB&CT<-15dB)	&1	
This work	TE_0-TE_1	9.39	/	<-15	<1	128/126	0.145	S
	TE_0-TE_2	11.27				(IL < 1dB&CT<-15dB)	&1	

[a]CE: Conversion efficiency CT: Crosstalk IL: Insertion loss
[a]E/S: Experiment/Simulation work MFS: Minimum feature size N: step of lithography and etching process

To further verify the scalability of our proposed scheme, we also demonstrate a TE_1–TE_2 MOC. The conversion between the TE_1 and TE_2 modes has been simulated using the optimized structure parameters listed in Table 3. The electric field distribution is shown in Fig. 9. It can be seen that the incident TE_1 mode can be converted to the TE_2 mode with a conversion length of 11.87 μm.

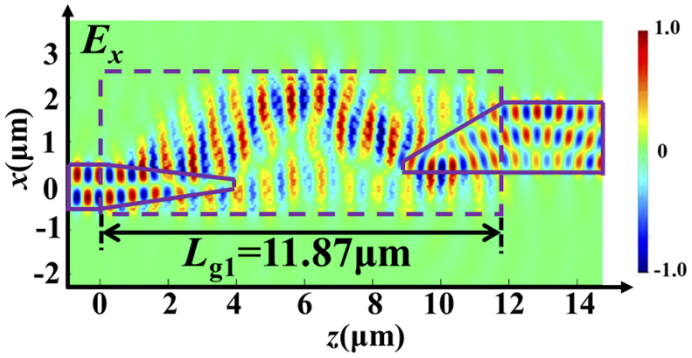

Fig. 9. Electric-field evolution with the simulated E_x distribution for the TE_1-TE_2 MOC

Optics EXPRESS

Table 3. Optimized design parameters for the proposed TE_1-TE_2 MOC

Mode converter	w_1 (μm)	w_2 (μm)	w_3 (μm)	w_4 (nm)	w_p (nm)	L_{tp1} (μm)	L_{tp2} (μm)	L_{g1} (μm)	$\overline{\Delta z}$
TE_1-TE_2	1	2.89	1.6	349	303	3.92	4.93	3.02	0.21

4. Conclusion

In conclusion, based on the mode evolution and coupling between the BSWG and the input/output asymmetric waveguide taper, a compact and broadband mode-order converter based on the BSWG is proposed. Two silicon-based MOCs employing the BSWG are demonstrated, which can convert the TE_0 mode to the TE_1 mode and TE_2 mode, respectively. The conversion lengths are 9.39 μm and 11.27 μm for the TE_0-TE_1 and TE_0-TE_2 MOCs, respectively. The broad design bandwidth of 128 nm (1511~1639 nm) and 126 nm (1527~1653 nm) are achieved with the conversion loss of <1 dB and the crosstalk value of <-15 dB for the TE_0-TE_1 and TE_0-TE_2 MOCs, with pixel size dimensions as large as 145×145 nm^2. Furthermore, our proposed scheme can be scaled to realize high-order waveguide mode conversions. We believe that the proposed mode order conversion scheme has potential applications in high-dense on-chip MDM systems and optical signal processing system.

Funding. National Key Research and Development Program of China (2018YFB2201800); National Natural Science Foundation of China (62105061, 62171118).

Disclosures. The authors declare no conflicts of interest.

Data availability. Data underlying the results presented in this paper are not publicly available at this time but may be obtained from the authors upon reasonable request.

References

1. R. Helkey, A. A. M. Saleh, J. Buckwalter, and J. E. Bowers, "High-performance photonic integrated circuits on silicon," IEEE J. Sel. Top. Quantum Electron. **25**(5), 1–15 (2019).
2. D. Dai and J. E. Bowers, "Silicon-based on-chip multiplexing technologies and devices for Peta-bit optical interconnects," Nanophotonics **3**(4-5), 283–311 (2014).
3. H. Li, P. Wang, T. Yang, T. Dai, G. Wang, S. Li, W. Chen, and J. Yang, "Experimental demonstration of a broadband two-mode multi/demultiplexer based on asymmetric Y-junctions," Opt. Laser Technol. **100**, 7–11 (2018).
4. T. H. Pan and S. Y. Tseng, "Short and robust silicon mode (de)multiplexers using shortcuts to adiabaticity," Opt. Express **23**(8), 10405–10412 (2015).
5. Y. Xu, L. Liu, X. Hu, Y. Dong, B. Zhang, and Y. Ni, "Scalable silicon-based mode-order converters assisted by tapered metal strip layer," Opt. Laser Technol. **151**, 108028 (2022).
6. D. Ohana and U. Levy, "Mode conversion based on dielectric metamaterial in silicon," Opt. Express **22**(22), 27617 (2014).
7. L. H. Gabrielli, D. Liu, S. G. Johnson, and M. Lipson, "On-chip transformation optics for multimode waveguide bends," Nat. Commun. **3**(1), 1217 (2012).
8. H. Xu and Y. Shi, "Ultra-sharp multi-mode waveguide bending assisted with metamaterial-based mode converters," Laser Photonics Rev. **12**(3), (2018).
9. W. Chang, L. Lu, X. Ren, L. Lu, M. Cheng, D. Liu, and M. Zhang, "An Ultracompact Multimode Waveguide Crossing Based on Subwavelength Asymmetric Y-Junction," IEEE Photonics J. **10**(4), 1–8 (2018).
10. Y. Xiong, D. Xu, J. H. Schmid, P. Cheben, S. Janz, and W. N. Ye, "Broadband two-mode multiplexer with taper-etched directional coupler on SOI platform," 11th International Conference on Group IV Photonics (GFP), Paris, 39–40 (2014).
11. W. Chen, P. Wang, and J. Yang, "Optical mode interleaver based on the asymmetric multimode Y junction," IEEE Photonics Technol. Lett. **26**(20), 2043–2046 (2014).
12. C. Sun, Y. Yu, G. Chen, and X. Zhang, "Integrated switchable mode exchange for reconfigurable mode- multiplexing optical networks," Opt. Lett. **41**(14), 3257–3260 (2016).
13. R. Xiao, Y. Shi, J. Li, P. Dai, Y. Zhao, L. Li, J. Lu, and X. Chen, "On-chip mode converter based on two cascaded Bragg gratings," Opt. Express **27**(3), 1941–1957 (2019).
14. L. Hao, R. Xiao, Y. Shi, P. Dai, Y. Zhao, S. Liu, J. Lu, and X. Chen, "Efficient TE-polarized mode-order converter based on high-index-contrast polygonal slot in a silicon-on-insulator waveguide," IEEE Photon. J. **11**(2), 1–10 (2019).
15. C.-C. Huang and C.-C. Huang, "Theoretical analysis of mode conversion by refractive-index perturbation based on a single tilted slot on a silicon waveguide," Opt. Express **28**(13), 18986–18999 (2020).

Optics EXPRESS

16. H. Wang, Y. Zhang, Y. He, Q. Zhu, L. Sun, and Y. Su, "Compact silicon waveguide mode converter employing dielectric metasurface structure," Adv. Opt. Mater. **7**(4), 1801191 (2018).
17. L. F. Frellsen, Y. Ding, O. Sigmund, and L. H. Frandsen, "Topology optimized mode multiplexing in silicon-on-insulator photonic wire waveguides," Opt. Express **24**(15), 16866–16873 (2016).
18. H. Jia, T. Zhou, X. Fu, J. Ding, and L. Yang, "Inverse-design and demonstration of ultracompact silicon meta-structure mode exchange device," ACS Photonics **5**(5), 1833–1838 (2018).
19. W. Ma, Z. Liu, Z. A. Kudyshev, A. Boltasseva, W. Cai, and Y. Liu, "Deep learning for the design of photonic structures," Nat. Photonics **15**(2), 77–90 (2021).
20. P. Cheben, D. X. Xu, S. Janz, and A. Densmore, "Subwavelength wave-guide grating for mode conversion and light coupling in integrated optics," Opt. Express **14**(11), 4695–4702 (2006).
21. P. Cheben, R. Halir, J. H. Schmid, H. A. Atwater, and D. R. Smith, "Sub-wavelength integrated photonics," Nature **560**(7720), 565–572 (2018).
22. L. Sun, Y. Zhang, Y. He, H. Wang, and Y. Su, "Subwavelength structured silicon waveguides and photonic devices," Nanophotonics **9**(6), 1321–1340 (2020).
23. Y. He, Y. Zhang, Q. Zhu, S. An, R. Cao, X. Guo, C. Qiu, and Y. Su, "Silicon high-Order mode (De)Multiplexer on single polarization," J. Lightwave Technol. **36**(24), 5746–5753 (2018).
24. W. Jiang, J. Miao, T. Li, and L. Ma, "Ultrabroadband and fabrication-tolerant mode (de)multiplexer using subwavelength structure," J. Opt. Soc. Am. B **36**(11), 3125 (2019).
25. L. Sun, R. Hu, Z. Zhang, Y. He, and Y. Su, "Ultrabroadband power coupling and mode-order conversion based on trapezoidal subwavelength gratings," IEEE J. of Sel. Topi. Quant. **27**(6), 1–8 (2021).
26. J. Manuel Luque-Gonzalez, A. Ortega-Monux, R. Halir, J. H. Schmid, P. Cheben, I. Molina-Fernandez, and J. Gonzalo Wanguemert-Perez, "Bricked subwavelength gratings: a tailorable on-chip metamaterial topology," Laser Photonics Rev. **15**(6), 2000478 (2021).
27. S. M. Rytov, "Electromagnetic properties of a finely stratified medium," Sov. Phys. Jetp. **2**(3), 466–475 (1956).
28. Z. Guo, S. Wu, and J. Xiao, "Compact and Flexible Mode-Order Converter Based on Mode Transitions Composed of Asymmetric Tapers and Subwavelength Gratings," J. Lightwave Technol. **39**(17), 5563–5572 (2021).
29. J. G. Wangümert-Pérez, P. Cheben, A. Ortega-Monux, C. Aloso-Ramos, and J. H. Schmid, "Evanescent field waveguide sensing with subwavelength grating structures in silicon-on-insulator," Opt. Lett. **39**(15), 4442–4445 (2014).
30. R. Yao, H. Li, B. Zhang, W. Chen, P. Wang, S. Dai, Y. Liu, J. Li, Y. Li, Q. Fu, T. Dai, H. Yu, J. Yang, and L. Pavesi, "Compact and low-insertion-loss 1×N power splitter in silicon photonics," J. Lightwave Technol. **39**(19), 6253–6259 (2021).